

# Atomic Layer Molecular Beam Epitaxy of Kagome Magnet $\text{RMn}_6\text{Sn}_6$ ( $\text{R} = \text{Er, Tb}$ ) Thin Films

Shuyu Cheng, Igor Lyalin, Wenyi Zhou, and Roland K. Kawakami<sup>a)</sup>

*Department of Physics, The Ohio State University, Columbus, Ohio 43210, United States*

Kagome lattices have garnered substantial interest because their band structure consists of topological flat bands and Dirac cones. The  $\text{RMn}_6\text{Sn}_6$  ( $\text{R} = \text{rare earth}$ ) compounds are particularly interesting because of the existence of large intrinsic anomalous Hall effect (AHE) which originates from the gapped Dirac cones near the Fermi level. This makes  $\text{RMn}_6\text{Sn}_6$  an outstanding candidate for realizing the high-temperature quantum anomalous Hall effect. The growth of  $\text{RMn}_6\text{Sn}_6$  thin films is beneficial for both fundamental research and potential applications. However, most of the studies on  $\text{RMn}_6\text{Sn}_6$  have focused on bulk crystals so far, and the synthesis of  $\text{RMn}_6\text{Sn}_6$  thin films has not been reported so far. Here we report the atomic layer molecular beam epitaxy growth, structural and magnetic characterizations, and transport properties of  $\text{ErMn}_6\text{Sn}_6$  and  $\text{TbMn}_6\text{Sn}_6$  thin films. It is especially noteworthy that  $\text{TbMn}_6\text{Sn}_6$  thin films have out-of-plane magnetic anisotropy, which is important for realizing the quantum anomalous Hall effect. Our work paves the avenue toward the control of the AHE using devices patterned from  $\text{RMn}_6\text{Sn}_6$  thin films.

Materials with layered kagome structures provide an ideal platform for studying the interplay between band structure and magnetism. In momentum space, a two-dimensional kagome lattice manifests Dirac cones at the K points<sup>1,2</sup>, saddle points at the M points<sup>3,4</sup>, and a flat band across the Brillouin zone<sup>5,6</sup>. The introduction of magnetism and spin-orbital coupling further opens a gap at the band touching points, leading to topologically non-trivial electronic states<sup>7-9</sup>. In real space, non-trivial spin textures (e.g. magnetic skyrmions) have been observed in kagome magnets<sup>10,11</sup>.

Recently,  $\text{RMn}_6\text{Sn}_6$  ( $\text{R} = \text{rare earth}$ ) compounds have emerged as a new family of topological kagome magnets<sup>12,13</sup>. The Mn atoms in  $\text{RMn}_6\text{Sn}_6$  form  $\text{Mn}_3$  kagome layers and the spin ordering of the  $\text{Mn}_3$  layers is largely affected by the R atoms. Previous studies on bulk crystals report that  $\text{R} = \text{Gd, Tb, Dy, and Ho}$  give rise to ferromagnetic coupling of Mn spins, while  $\text{R} = \text{Er, Tm, and Lu}$  lead to antiferromagnetic coupling of Mn spins at zero field<sup>14-16</sup>. Rare earth elements in  $\text{RMn}_6\text{Sn}_6$  compounds also provide one additional knob for tuning the magnetocrystalline anisotropy (MCA) which is connected to the Dirac gap opening<sup>17</sup>. Large Berry-curvature-induced intrinsic anomalous Hall effect (AHE) may originate from the gapped Dirac cones close to the Fermi level, because the intrinsic anomalous Hall conductivity (AHC) is connected to the Dirac gap opening  $\Delta$  and the Dirac cone position  $E_D$  through<sup>18</sup>:

$$\sigma^{int} = \frac{e^2}{h} \frac{\Delta}{2E_D} \quad (1)$$

Notably,  $\text{TbMn}_6\text{Sn}_6$  bulk crystals exhibit out-of-plane magnetic anisotropy, which leads to a 34 meV Dirac gap opening at 130 meV above the Fermi level<sup>12</sup>, and band structure calculations predict the quantum anomalous

Hall effect (QAHE) if the Fermi level could be tuned into the gap. Experimentally, the observation of a giant intrinsic AHC of  $\sigma^{int}=0.14 e^2/h$  per kagome layer in  $\text{TbMn}_6\text{Sn}_6$  bulk crystals<sup>12</sup> makes the  $\text{RMn}_6\text{Sn}_6$  family of materials attractive for QAHE. To this end, the growth of  $\text{RMn}_6\text{Sn}_6$  thin films provides opportunities for tuning the band structure and Fermi level through epitaxial strain, chemical doping, or voltage gating. However, all of the reported works have focused on bulk crystals of  $\text{RMn}_6\text{Sn}_6$ , while studies on their thin film counterparts have been missing. Therefore, the development of epitaxial  $\text{RMn}_6\text{Sn}_6$  thin films is highly desired.

In this paper, we report the growth of (0001)-oriented thin films of  $\text{ErMn}_6\text{Sn}_6$  and  $\text{TbMn}_6\text{Sn}_6$  using atomic layer molecular beam epitaxy (AL-MBE) and characterize their magnetic and transport properties. The films are grown on Pt(111) buffer layers on  $\text{Al}_2\text{O}_3(0001)$  substrates. Various methods are employed to characterize the structure of our samples, including *in-situ* reflection high energy electron diffraction (RHEED), X-ray diffraction (XRD), and atomic force microscopy (AFM). We demonstrate that the magnetic properties of  $\text{RMn}_6\text{Sn}_6$  thin films can be tuned through the selection of rare earth element  $R$ .  $\text{ErMn}_6\text{Sn}_6$  thin films favor in-plane (IP) magnetization, while  $\text{TbMn}_6\text{Sn}_6$  thin films undergo an out-of-plane (OOP) to IP spin-reorientation transition (SRT) as the temperature increases above 300 K. Lastly, we find that the longitudinal resistance of  $\text{RMn}_6\text{Sn}_6/\text{Pt}$  bilayers do not follow a simple parallel resistor model but instead depends on the electron mean free path and can be explained qualitatively by the Fuchs-Sondheimer model.

The crystal structure of  $\text{RMn}_6\text{Sn}_6$  is displayed in Fig. 1, featuring a hexagonal lattice (space group  $P6/mmm$ , lattice constants  $a = 5.5 \text{ \AA}$  and  $c = 9.0 \text{ \AA}$ ) with atomic layers stacked along the  $c$ -axis<sup>19</sup>. In each unit cell, there are two kagome  $\text{Mn}_3$  layers closely neighbored by two  $\text{Sn}_1$  layers, with one honeycomb  $\text{Sn}_2$  layer inserted between two  $\text{Sn}_1$  layers, and one  $\text{RSn}_2$  layer inserted between  $\text{Mn}_3$  kagome layers. Inspired by this

<sup>a)</sup>Electronic mail: kawakami.15@osu.edu

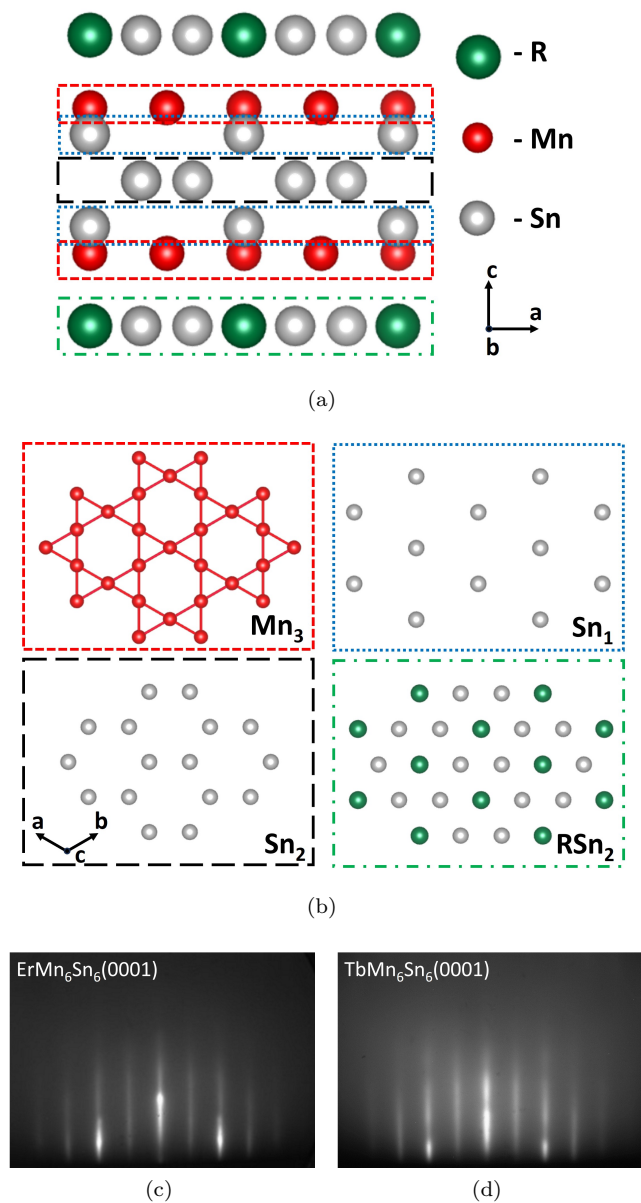


FIG. 1. AL-MBE Growth of  $RMn_6Sn_6$  thin films. (a). Lattice structure of  $RMn_6Sn_6$  viewed from the side. In each unit cell,  $RMn_6Sn_6$  consists of alternating stacking of  $RSn_2$ ,  $Mn_3$ ,  $Sn_1$ ,  $Sn_2$ ,  $Sn_1$ ,  $Mn_3$  layers (from bottom to top) along c-axis. (b). In-plane lattice structure of kagome  $Mn_3$  (top left), triangular  $Sn_1$  (top right), honeycomb  $Sn_2$  (bottom left), and  $RSn_2$  (bottom right) layers. (c, d). *in-situ* RHEED pattern of 20 nm  $ErMn_6Sn_6$  sample grown on Pt(111) buffer layer on  $Al_2O_3(0001)$  substrate. (d). *in-situ* RHEED pattern of 20 nm  $TbMn_6Sn_6$  sample grown on Pt(111) buffer layer on  $Al_2O_3(0001)$  substrate.

stacking sequence, we develop an AL-MBE recipe to grow  $ErMn_6Sn_6$  and  $TbMn_6Sn_6$  thin films on epitaxial Pt(111) buffer layers on  $Al_2O_3(0001)$  substrates. In AL-MBE, atomic layers are grown sequentially by opening and closing the appropriate MBE source shutters with precise timing. A similar growth strategy allowed us to synthe-

size thin films of another kagome magnet,  $Fe_3Sn_2$ , which also has a hexagonal layered lattice structure<sup>20</sup>.

The base pressure of the growth chamber is  $1 \times 10^{-9}$  Torr. The  $Al_2O_3(0001)$  substrates (MTI corporation) are annealed in air at  $1000^\circ C$  for 3 hours, then degassed *in-situ* at  $500^\circ C$  for 30 minutes to prepare a flat and clean surface. A 5 nm epitaxial Pt(111) buffer layer is subsequently grown on  $Al_2O_3(0001)$  following the recipe described in our previous work<sup>20</sup>. The  $ErMn_6Sn_6(0001)$  and  $TbMn_6Sn_6(0001)$  thin films are grown on Pt(111) buffer layers at  $100^\circ C$  and  $80^\circ C$ , respectively using the AL-MBE recipe described below. First, the kagome  $Mn_3$  layer and hexagonal  $Sn_1$  layer are co-deposited with flux ratio  $Mn:Sn = 3:1$ , then the honeycomb  $RSn_2$  is deposited with flux ratio  $Er:Sn$  (or  $Tb:Sn$ ) =  $2:1$ , then another hexagonal  $Sn_1$  layer and kagome  $Mn_3$  layer are co-deposited, then one  $Sn_2$  layer is deposited. The aforementioned shutter growth sequence is repeated until the desired thickness (typically 20 nm) of  $RMn_6Sn_6$  is achieved. Typical deposition rates are  $1.6 \text{ \AA}/\text{min}$ ,  $1.6 \text{ \AA}/\text{min}$ ,  $3.9 \text{ \AA}/\text{min}$ , and  $2.8 \text{ \AA}/\text{min}$  for Er, Tb, Mn, and Sn, respectively. After growth, a 5 nm  $CaF_2$  layer is deposited to prevent sample oxidation.

The *in-situ* RHEED patterns of  $ErMn_6Sn_6$  and  $TbMn_6Sn_6$  are monitored during the growths. The RHEED patterns of a 20 nm  $ErMn_6Sn_6$  thin film and a 20 nm  $TbMn_6Sn_6$  thin film along  $Al_2O_3[11\bar{2}0]$  direction are shown in Fig. 1c and 1d, respectively. The RHEED patterns are generally streaky, suggesting the morphology of our  $RMn_6Sn_6$  thin films is dominated by two-dimensional terraces with finite sizes, although some three-dimensional features also exist as spots. The RHEED pattern suggests the in-plane lattice constants for our samples are  $a_{ErMn_6Sn_6} = 5.47 \text{ \AA}$ , and  $a_{TbMn_6Sn_6} = 5.56 \text{ \AA}$ , respectively, and the in-plane epitaxial relationship is  $RMn_6Sn_6[1\bar{1}00] \parallel Pt[110] \parallel Al_2O_3[11\bar{2}0]$ .

We perform XRD measurements to confirm the crystallographic structures of  $ErMn_6Sn_6$  and  $TbMn_6Sn_6$  thin films. The X-ray is from the Cu-K $\alpha$  radiation, with a wavelength of  $1.5406 \text{ \AA}$ . Fig. 2a shows the XRD data of a 20 nm  $ErMn_6Sn_6$  thin film. Next to the substrate peaks at  $41.57^\circ$  and  $90.60^\circ$ , two major peaks are found at  $39.78^\circ$  and  $85.46^\circ$ , respectively. These peaks are attributed to Pt(111) and Pt(222) peaks because their  $2\theta$  angles convert to out-of-plane lattice constants of  $2.275 \text{ \AA}$  and  $2.270 \text{ \AA}$ , respectively. These values are close to the out-of-plane lattice constant of Pt along (111) direction ( $\sqrt{3}/3 \times 3.923 \text{ \AA} = 2.265 \text{ \AA}$ )<sup>21</sup>.  $ErMn_6Sn_6(0004)$  and  $ErMn_6Sn_6(0008)$  peaks appear as nearby shoulder peaks at  $40.36^\circ$  and  $87.63^\circ$ , respectively. The out-of-plane lattice constant of  $ErMn_6Sn_6$  extracted from (0004) peak is  $8.93 \text{ \AA}$ , which is close to but slightly smaller than the reported bulk value of  $9.0006 \text{ \AA}$ <sup>22</sup>.

For  $TbMn_6Sn_6$  thin film, the general characteristics of the XRD data are similar to  $ErMn_6Sn_6$ . To the right of Pt(111) peak which is at  $39.88^\circ$ , the  $TbMn_6Sn_6(0004)$  peak is found as a shoulder peak (see Fig. 2c). A double Gaussian peak fitting yields  $TbMn_6Sn_6(0004)$  peak

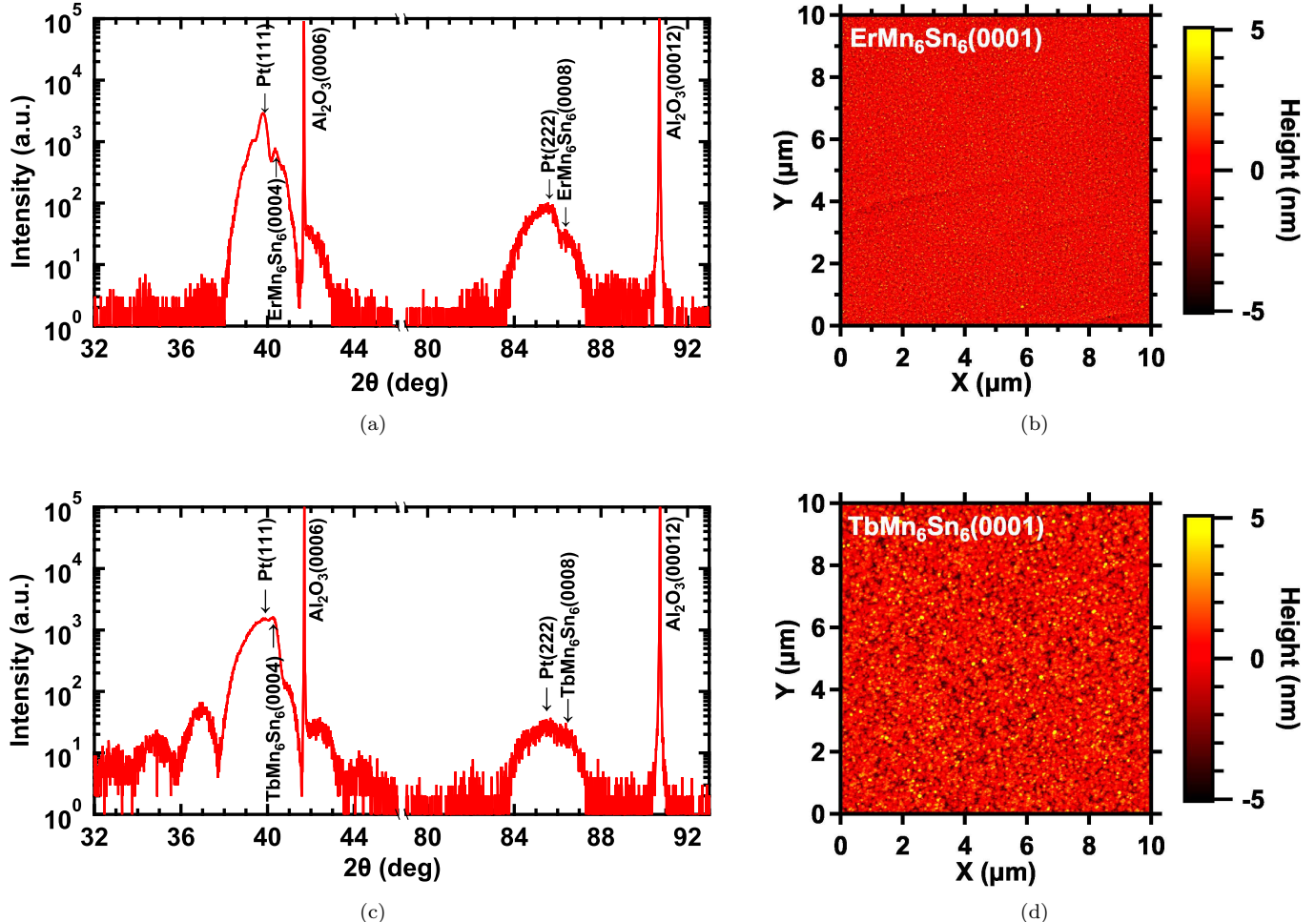


FIG. 2. Structural characterizations of  $RMn_6Sn_6$  thin films. (a). XRD data of  $ErMn_6Sn_6(20\text{ nm})/Pt(5\text{ nm})$  sample. (b). AFM image of  $ErMn_6Sn_6(20\text{ nm})/Pt(5\text{ nm})$  sample. (c). XRD data of  $TbMn_6Sn_6(25\text{ nm})/Pt(5\text{ nm})$  sample. (d). AFM image of  $TbMn_6Sn_6(25\text{ nm})/Pt(5\text{ nm})$  sample.

position of  $40.26^\circ$ , which corresponds to an out-of-plane lattice of  $c = 8.95\text{ \AA}$ . This is also smaller than the reported bulk value of  $9.0208\text{ \AA}^{22}$ .

We characterize the surface morphology of  $ErMn_6Sn_6$  and  $TbMn_6Sn_6$  thin films using AFM. Fig. 2b shows the AFM image of a 20 nm  $ErMn_6Sn_6$  sample grown at  $100^\circ\text{C}$ . The film has a continuous and flat surface with sub-micron grain size. The root-mean-square (rms) roughness of the 20 nm  $ErMn_6Sn_6$  sample is 1.02 nm. Fig. 2b shows the AFM image of a 20 nm  $TbMn_6Sn_6$  sample grown at  $80^\circ\text{C}$ . The rms roughness of the 20 nm  $TbMn_6Sn_6$  sample is 1.45 nm.

To investigate the magnetic properties of the  $RMn_6Sn_6$  thin films, we perform SQUID magnetometer measurements. Fig. 3a shows the IP (blue) and OOP (red) hysteresis loops of a 20 nm  $ErMn_6Sn_6$  thin film. The IP hysteresis loop has a smaller saturation field of 0.2 Tesla, while the OOP hysteresis loop has a larger saturation field of 1.7 Tesla, indicating  $ErMn_6Sn_6$  has easy-plane

anisotropy at room temperature. The saturation magnetization of  $ErMn_6Sn_6$  thin film is  $5.4\mu_B/\text{f.u.}$  ( $212\text{ kA/m}$ ) at room temperature. The IP and OOP hysteresis loops of  $ErMn_6Sn_6$  at  $T = 5\text{ K}$  are shown in Fig. 3b. At  $T = 5\text{ K}$ , both IP and OOP hysteresis loops show much larger coercive fields and larger saturation fields, while the saturation field of the OOP hysteresis loop is still larger than the IP hysteresis loop. The IP loop exhibits a sharper switching behavior, with the coercive field of 0.47 Tesla. Meanwhile, the OOP hysteresis loop becomes narrower near zero field and wider at higher fields. The coercive field of the OOP hysteresis loop is 0.30 Tesla.

We also measure the temperature-dependence of remanence magnetization of the  $ErMn_6Sn_6$  thin film, as shown in Fig. 3c. For both OOP (the red curve) and IP (the blue curve) measurements, the sample is cooled down under 7 Tesla applied field, and measured at low field while heating up. A 30 mT field is applied to set the polarity of the magnetization. From the temperature-dependent

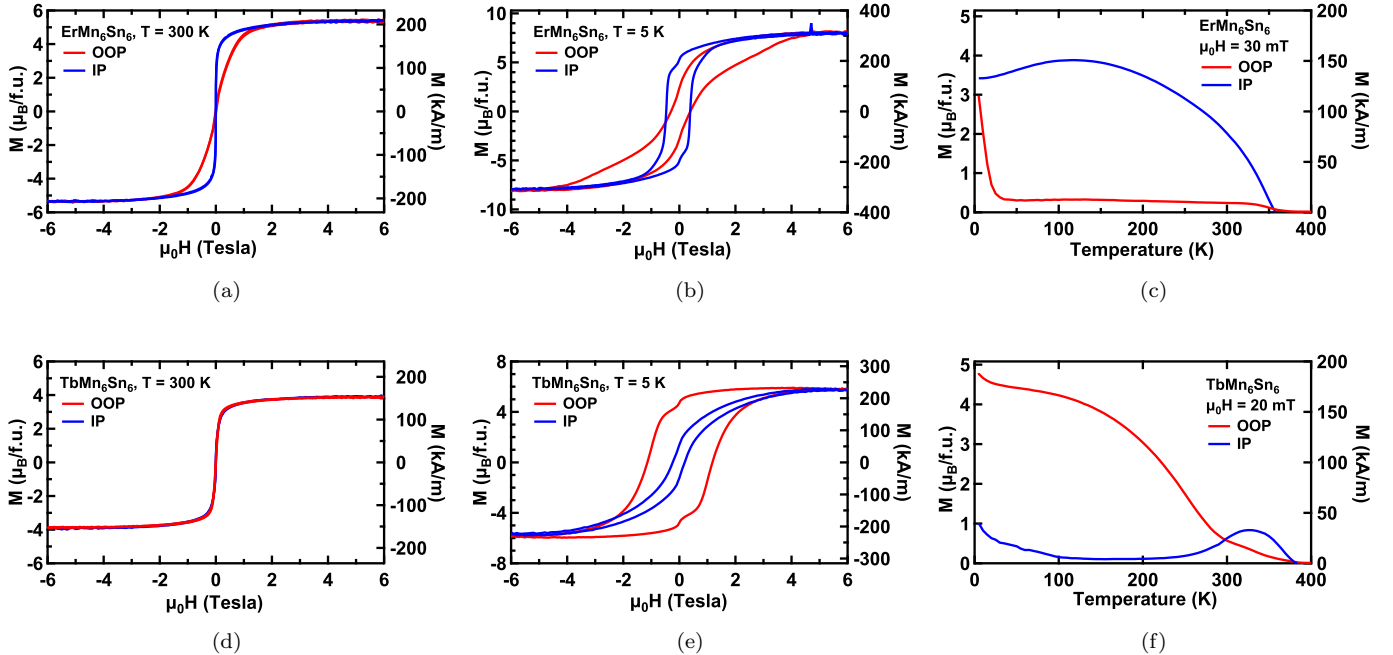


FIG. 3. Magnetic properties of ErMn<sub>6</sub>Sn<sub>6</sub> and TbMn<sub>6</sub>Sn<sub>6</sub> thin films. (a - c). Magnetic properties of 20 nm ErMn<sub>6</sub>Sn<sub>6</sub> thin film measured with out-of-plane (OOP, red) and in-plane (IP, blue) geometries. (a). M vs. H hysteresis loops measured at T=300 K. (b). M vs. H hysteresis loop measured at T=5 K. (c). M vs. T curve. (d - f). Magnetic properties of 20 nm TbMn<sub>6</sub>Sn<sub>6</sub> thin film measured with out-of-plane (OOP, red) and in-plane (IP, blue) geometries. (d). M vs. H hysteresis loops measured at T=300 K. (e). M vs. H hysteresis loop measured at T=5 K. (f). M vs. T curve, showing uniaxial anisotropy for T<sub>i</sub>300 and an OOP-to-IP spin reorientation at T=300 K.

magnetization curve, the Curie temperature of the 20 nm ErMn<sub>6</sub>Sn<sub>6</sub> thin film is determined to be 353 K, signified by a drop of magnetization to zero. This Curie temperature is consistent with the reported value of 350 K on ErMn<sub>6</sub>Sn<sub>6</sub> bulk crystals<sup>16</sup>.

Compared to ErMn<sub>6</sub>Sn<sub>6</sub> thin films, TbMn<sub>6</sub>Sn<sub>6</sub> thin films show different magnetic properties. Fig. 3d and 3e show the hysteresis loops of a 25 nm TbMn<sub>6</sub>Sn<sub>6</sub> thin film at 300 K and 5 K, respectively. At T = 300 K, the OOP (red) and IP (blue) hysteresis loops of TbMn<sub>6</sub>Sn<sub>6</sub> are almost identical, with a saturation field of 0.6 Tesla (see Fig. 3d). The saturation magnetization of TbMn<sub>6</sub>Sn<sub>6</sub> is  $3.9 \mu_B/\text{f.u.}$  (154 kA/m) at room temperature. While cooling down to T = 5 K, the OOP hysteresis loop of TbMn<sub>6</sub>Sn<sub>6</sub> exhibits a square shape, with tails extended to 5 Tesla, as shown in Fig. 3e. Meanwhile, the IP hysteresis loop shows a gradual switching behavior. At zero field, the OOP remanence magnetization is much larger than the IP remanence magnetization, suggesting that TbMn<sub>6</sub>Sn<sub>6</sub> favors OOP at T = 5 K.

The perpendicular magnetic anisotropy is highly unusual for epitaxial kagome magnet thin films, as most of the previously reported kagome magnet thin films have easy-plane anisotropy<sup>20,23-27</sup>. Even for epitaxial Fe<sub>3</sub>Sn<sub>2</sub> whose bulk form has MCA along the c-axis, the MCA is overcome by the magnetic shape anisotropy (MSA) which favors easy-plane anisotropy. As a result, both

MBE-grown and sputtered Fe<sub>3</sub>Sn<sub>2</sub> thin films manifest easy-plane anisotropy<sup>20,25</sup>. However, in TbMn<sub>6</sub>Sn<sub>6</sub> thin films, the MCA is strong enough to overcome the MSA and leads to an easy-axis anisotropy at low temperatures. It is noteworthy that such large magnetocrystalline anisotropy along the c-axis opens a gap at the Dirac cone, leading to a large intrinsic AHE<sup>12,13</sup>.

The perpendicular magnetic anisotropy of the TbMn<sub>6</sub>Sn<sub>6</sub> thin film sample at low temperatures is further confirmed by the temperature-dependent SQUID measurements, as shown in Fig. 3f. A 20 mT field is applied to set the polarity of the magnetization. Below 300 K, the OOP magnetization (red curve) is always larger than the IP magnetization (blue curve). A crossover between IP and OOP magnetization happens at T = 300 K above which the IP magnetization becomes larger than the OOP magnetization. This crossover suggests an OOP-to-IP SRT as the temperature increases above 300 K. A similar temperature-induced SRT has been observed at 310 K in TbMn<sub>6</sub>Sn<sub>6</sub> bulk crystals<sup>16</sup> and is reported to be related to the formation of magnetic skyrmions<sup>11</sup>. Both IP and OOP magnetization eventually disappears above the Curie temperature which is determined to be 380 K. This Curie temperature is lower than the reported value of 423 K on TbMn<sub>6</sub>Sn<sub>6</sub> bulk crystals<sup>14</sup>.

We next discuss the transport properties of

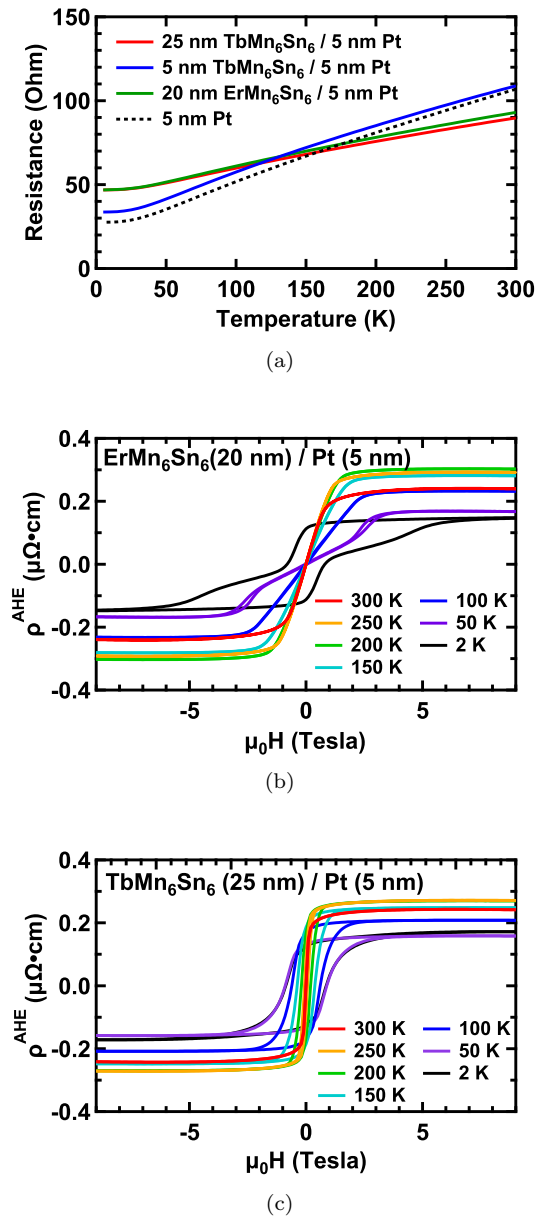


FIG. 4. Transport measurements of  $\text{ErMn}_6\text{Sn}_6/\text{Pt}$  and  $\text{TbMn}_6\text{Sn}_6/\text{Pt}$  bilayers. (a). Resistance of  $300\ \mu\text{m} \times 100\ \mu\text{m}$  devices patterned from  $\text{TbMn}_6\text{Sn}_6(25\ \text{nm})/\text{Pt}(5\ \text{nm})$  bilayer (red),  $\text{TbMn}_6\text{Sn}_6(5\ \text{nm})/\text{Pt}(5\ \text{nm})$  bilayer (blue),  $\text{ErMn}_6\text{Sn}_6(20\ \text{nm})/\text{Pt}(5\ \text{nm})$  bilayer, and  $5\ \text{nm}$  Pt single layer (black, dashed), respectively. (b). Anomalous Hall resistivity of  $\text{ErMn}_6\text{Sn}_6(20\ \text{nm})/\text{Pt}(5\ \text{nm})$  bilayer measured at different temperatures ranging from 2 K to 300 K. (c). Anomalous Hall resistivity of  $\text{TbMn}_6\text{Sn}_6(25\ \text{nm})/\text{Pt}(5\ \text{nm})$  bilayer measured at different temperatures ranging from 2 K to 300 K.

$\text{ErMn}_6\text{Sn}_6/\text{Pt}$  and  $\text{TbMn}_6\text{Sn}_6/\text{Pt}$  thin films. The transport measurements are performed using Quantum Design Physical Property Measurement System (PPMS) on  $300\ \mu\text{m} \times 100\ \mu\text{m}$  Hall bar devices patterned from  $\text{ErMn}_6\text{Sn}_6/\text{Pt}$  and  $\text{TbMn}_6\text{Sn}_6/\text{Pt}$  thin films. The longitudinal resistance of the Hall bar devices at

zero field is shown in Fig. 4a. Comparing between  $\text{TbMn}_6\text{Sn}_6(25\ \text{nm})/\text{Pt}(5\ \text{nm})$  bilayer (the red curve) and  $\text{Pt}(5\ \text{nm})$  single layer (the black dashed curve), the bilayer resistance is lower than the Pt single layer resistance for higher temperatures ( $T > 200\ \text{K}$ ). This is consistent with the parallel resistor model in which the  $\text{TbMn}_6\text{Sn}_6$  and Pt layers are modeled as two resistors connected in parallel and therefore have smaller resistance than the Pt layer alone. The parallel resistor model has been widely used to extract the resistivity of kagome material thin films grown on metallic buffer layers<sup>24–26,28</sup>. However, at low temperatures ( $T < 150\ \text{K}$ ), the resistance of the  $\text{TbMn}_6\text{Sn}_6(25\ \text{nm})/\text{Pt}(5\ \text{nm})$  bilayer is larger than that of the  $\text{Pt}(5\ \text{nm})$  single layer. This is the opposite of what one would expect from the parallel resistor model. The comparison between  $\text{ErMn}_6\text{Sn}_6(20\ \text{nm})/\text{Pt}(5\ \text{nm})$  bilayer (the green curve) and  $\text{Pt}(5\ \text{nm})$  single layer shows a similar trend that the bilayer resistance is smaller than the Pt single layer resistance for  $T > 200\ \text{K}$  and larger than the Pt single layer resistance for  $T < 100\ \text{K}$ . The deviation from the parallel resistor model is more pronounced for the bilayers with smaller kagome layer thicknesses. For example, for  $\text{TbMn}_6\text{Sn}_6(5\ \text{nm})/\text{Pt}(5\ \text{nm})$  bilayer (the blue curve), the resistance is larger than  $\text{Pt}(5\ \text{nm})$  single layer from  $T = 5\ \text{K}$  up to  $T = 300\ \text{K}$ .

The deviation from the parallel resistor model can be explained by Fuchs-Sondheimer theory, in which the resistance of bilayers depends not only on the bulk resistance of two materials but also the mean free path of electrons in them<sup>29,30</sup>. In the Fuchs-Sondheimer model, when the electron mean free path is much smaller than the thickness of each layer, the bilayer resistance is smaller than the resistance of individual layers. In this case, the Fuchs-Sondheimer model converges to the parallel resistor model. However, when the electron mean free path is much larger than the thickness of each layer, the bilayer resistance is larger than the resistance of individual layers, which is more similar to the series resistor model. Especially in an infinite superlattice consisting of alternating stacking of two materials with the same thickness, in the thin layer limit and under the assumption that the electron densities in two materials are identical, the averaged resistivity of the superlattice is exactly equal to the average value of the bulk resistivity of the two materials<sup>31</sup>. In our  $\text{RMn}_6\text{Sn}_6/\text{Pt}$  bilayer samples, the scattering length is shorter than the individual layer thickness at high temperatures, therefore the bilayer resistance is smaller than the resistance of Pt layer, similar to the parallel resistor model. Meanwhile, at low temperatures or with smaller thicknesses, the mean free path becomes longer than the individual layer thickness, and the bilayer resistance is larger than the resistance of Pt layer, similar to the series resistor model. Due to the complexity of data analysis, extracting the intrinsic longitudinal resistivity of  $\text{ErMn}_6\text{Sn}_6$  and  $\text{TbMn}_6\text{Sn}_6$  from bilayer resistance is outside the scope of this paper.

We also measured the anomalous Hall ef-

fect (AHE) of  $\text{ErMn}_6\text{Sn}_6(20\text{ nm})/\text{Pt}(5\text{ nm})$  and  $\text{TbMn}_6\text{Sn}_6(25\text{ nm})/\text{Pt}(5\text{ nm})$  bilayers, as shown in Fig. 4b and Fig. 4c, respectively. Here, the anomalous Hall resistivity is calculated by multiplying the anomalous Hall resistance by the thickness of the  $\text{RMn}_6\text{Sn}_6$  layer. For  $\text{ErMn}_6\text{Sn}_6$ , the AHE hysteresis loop at  $T = 2\text{ K}$  has a large remanence, a low-field opening (with the coercive field of  $\sim 1\text{ T}$ ) and a large saturation field ( $\sim 6\text{ T}$ ). The opening of the hysteresis loop decreases quickly as the temperature increases, and almost disappears before the temperature reaches  $100\text{ K}$ . For  $\text{TbMn}_6\text{Sn}_6$ , the AHE hysteresis loops are relatively square, with the coercive field decreasing as temperature increases. For both materials, as temperature increases from  $2\text{ K}$  to  $300\text{ K}$ , the amplitude of AHE first increases, reaches the maximum value between  $200\text{ K}$  and  $250\text{ K}$ , and then decreases. This behavior is understood as follows. The anomalous Hall resistivity  $\rho^{AH}$  scales with  $\rho_{xx}^\alpha$  where  $\alpha$  is between 1 and 2. The intrinsic and side-jump contributions yield  $\alpha = 2$  and skew-scattering yields  $\alpha = 1$ .<sup>32</sup> Since  $\rho_{xx}$  increases with temperature (Figure 4a), this scaling explains the enhancement of  $\rho^{AH}$  with temperature as observed below  $200\text{ K}$ . On the other hand, the reduction of AHE resistivity at higher temperatures can be attributed to the decrease in magnetization as the temperature approaches the Curie temperature.

In conclusion, this study demonstrates the synthesis of *c*-plane  $\text{ErMn}_6\text{Sn}_6$  and  $\text{TbMn}_6\text{Sn}_6$  thin films using atomic layer molecular beam epitaxy. A combination of RHEED, XRD, and AFM confirms the structure of the samples. Magnetization measurements show that  $\text{ErMn}_6\text{Sn}_6$  has easy-plane anisotropy from  $5\text{ K}$  to room temperature, while  $\text{TbMn}_6\text{Sn}_6$  has perpendicular magnetic anisotropy at low temperature and an OOP-to-IP spin reorientation as the temperature increases above  $300\text{ K}$ . Transport measurements at low temperatures show that the longitudinal resistance of the  $\text{RMn}_6\text{Sn}_6/\text{Pt}$  bilayer is larger than that of the Pt layer alone, which is inconsistent with the parallel resistance model. On the other hand, such behavior is qualitatively explained by the Fuchs-Sondheimer model. Lastly, since both  $\text{ErMn}_6\text{Sn}_6$  and  $\text{TbMn}_6\text{Sn}_6$  are synthesized under similar conditions, other members of the  $\text{RMn}_6\text{Sn}_6$  family could likely be grown using similar AL-MBE recipes. These results create a solid foundation for future research and applications based on  $\text{RMn}_6\text{Sn}_6$  thin films.

## ACKNOWLEDGMENTS

We acknowledge Daniel Halbing, Katherine Robinson, and Xueshi Gao for their assistance in the construction of the evaporation cells. S.C. was supported by NSF Grant No. CHE-1935885. I.L. was supported by the Center for Emergent Materials, an NSF MRSEC, under Grant No. DMR-2011876. W.Z. was supported by AFOSR MURI 2D MAGIC Grant No. FA9550-19-1-0390 and the US

Department of Energy Grant No. DE-SC0016379.

## AUTHOR DECLARATIONS

### Conflict of Interest

The authors declare no conflicts of interest to disclose.

## DATA AVAILABILITY STATEMENT

The data that support the findings of this study are available from the corresponding author upon reasonable request.

## REFERENCES

- <sup>1</sup>K. Kuroda, T. Tomita, M.-T. Suzuki, C. Bareille, A. Nugroho, P. Goswami, M. Ochi, M. Ikhlas, M. Nakayama, S. Akebi, R. Noguchi, R. Ishii, N. Inami, K. Ono, H. Kumigashira, A. Varykhalov, T. Muro, T. Koretsune, R. Arita, S. Shin, T. Kondo, and S. Nakatsuji, "Evidence for magnetic Weyl fermions in a correlated metal," *Nature materials* **16**, 1090–1095 (2017).
- <sup>2</sup>L. Ye, M. Kang, J. Liu, F. Von Cube, C. R. Wicker, T. Suzuki, C. Jozwiak, A. Bostwick, E. Rotenberg, D. C. Bell, L. Fu, R. Comin, and J. G. Checkelsky, "Massive Dirac fermions in a ferromagnetic kagome metal," *Nature* **555**, 638–642 (2018).
- <sup>3</sup>M. Kang, S. Fang, J.-K. Kim, B. R. Ortiz, S. H. Ryu, J. Kim, J. Yoo, G. Sangiovanni, D. Di Sante, B.-G. Park, C. Jozwiak, A. Bostwick, E. Rotenberg, E. Kaxiras, S. D. Wilson, J.-H. Park, and R. Comin, "Twofold van Hove singularity and origin of charge order in topological kagome superconductor  $\text{CsV}_3\text{Sb}_5$ ," *Nature Physics* **18**, 301–308 (2022).
- <sup>4</sup>X. Teng, J. S. Oh, H. Tan, L. Chen, J. Huang, B. Gao, J.-X. Yin, J.-H. Chu, M. Hashimoto, D. Lu, C. Jozwiak, A. Bostwick, E. Rotenberg, G. E. Granroth, B. Yan, R. J. Birgeneau, P. Dai, and M. Yi, "Magnetism and charge density wave order in kagome  $\text{FeGe}$ ," *Nature Physics*, 1–9 (2023).
- <sup>5</sup>M. Kang, S. Fang, L. Ye, H. C. Po, J. Denlinger, C. Jozwiak, A. Bostwick, E. Rotenberg, E. Kaxiras, J. G. Checkelsky, and R. Comin, "Topological flat bands in frustrated kagome lattice  $\text{CoSn}$ ," *Nature communications* **11**, 4004 (2020).
- <sup>6</sup>M. Kang, L. Ye, S. Fang, J.-S. You, A. Levitan, M. Han, J. I. Facio, C. Jozwiak, A. Bostwick, E. Rotenberg, M. K. Chan, R. D. McDonald, D. Graf, K. Kaznatcheev, E. Vescovo, D. C. Bell, E. Kaxiras, J. van den Brink, M. Richter, M. P. Ghimire, C. J. G., and R. Comin, "Dirac fermions and flat bands in the ideal kagome metal  $\text{FeSn}$ ," *Nature materials* **19**, 163–169 (2020).
- <sup>7</sup>K. Sun, Z. Gu, H. Katsura, and S. D. Sarma, "Nearly flatbands with nontrivial topology," *Physical Review Letters* **106**, 236803 (2011).
- <sup>8</sup>H.-M. Guo and M. Franz, "Topological insulator on the kagome lattice," *Physical Review B* **80**, 113102 (2009).
- <sup>9</sup>A. Bolens and N. Nagaosa, "Topological states on the breathing kagome lattice," *Physical Review B* **99**, 165141 (2019).
- <sup>10</sup>Z. Hou, W. Ren, B. Ding, G. Xu, Y. Wang, B. Yang, Q. Zhang, Y. Zhang, E. Liu, F. Xu, W. Wang, G. Wu, X. Zhang, B. Shen, and Z. Zhang, "Observation of various and spontaneous magnetic skyrmionic bubbles at room temperature in a frustrated kagome magnet with uniaxial magnetic anisotropy," *Advanced Materials* **29**, 1701144 (2017).

- <sup>11</sup>Z. Li, Q. Yin, Y. Jiang, Z. Zhu, Y. Gao, S. Wang, J. Shen, T. Zhao, J. Cai, H. Lei, S.-Z. Lin, Y. Zhang, and B. Shen, "Discovery of topological magnetic textures near room temperature in quantum magnet  $\text{TbMn}_6\text{Sn}_6$ ," *Advanced Materials*, 2211164 (2023).
- <sup>12</sup>J.-X. Yin, W. Ma, T. A. Cochran, X. Xu, S. S. Zhang, H.-J. Tien, N. Shumiya, G. Cheng, K. Jiang, B. Lian, Z. Song, G. Chang, I. Belopolski, D. Multer, M. Litskevich, Z.-J. Cheng, X. P. Yang, B. Swidler, H. Zhou, H. Lin, T. Neupert, Z. Wang, N. Yao, T.-R. Chang, S. Jia, and M. Z. Hasan, "Quantum-limit Chern topological magnetism in  $\text{TbMn}_6\text{Sn}_6$ ," *Nature* **583**, 533–536 (2020).
- <sup>13</sup>W. Ma, X. Xu, J.-X. Yin, H. Yang, H. Zhou, Z.-J. Cheng, Y. Huang, Z. Qu, F. Wang, M. Z. Hasan, and S. Jia, "Rare earth engineering in  $\text{RMn}_6\text{Sn}_6$  ( $R = \text{Gd} - \text{Tm}, \text{Lu}$ ) topological kagome magnets," *Physical review letters* **126**, 246602 (2021).
- <sup>14</sup>G. Venturini, B. C. El Idrissi, and B. Malaman, "Magnetic properties of  $\text{RMn}_6\text{Sn}_6$  ( $R = \text{Sc}, \text{Y}, \text{Gd}-\text{Tm}, \text{Lu}$ ) compounds with  $\text{HfFe}_6\text{Ge}_6$  type structure," *Journal of magnetism and magnetic materials* **94**, 35–42 (1991).
- <sup>15</sup>B. Malaman, G. Venturini, R. Welter, J. Sanchez, P. Vulliet, and E. Ressouche, "Magnetic properties of  $\text{RMn}_6\text{Sn}_6$  ( $R = \text{Gd}-\text{Er}$ ) compounds from neutron diffraction and Mössbauer measurements," *Journal of magnetism and magnetic materials* **202**, 519–534 (1999).
- <sup>16</sup>D. Clatterbuck and K. Gschneidner Jr, "Magnetic properties of  $\text{RMn}_6\text{Sn}_6$  ( $R = \text{Tb}, \text{Ho}, \text{Er}, \text{Tm}, \text{Lu}$ ) single crystals," *Journal of magnetism and magnetic materials* **207**, 78–94 (1999).
- <sup>17</sup>Z.-J. Cheng, I. Belopolski, H.-J. Tien, T. A. Cochran, X. P. Yang, W. Ma, J.-X. Yin, D. Chen, J. Zhang, C. Jozwiak, *et al.*, "Visualization of tunable Weyl line in A–A stacking kagome magnets," *Advanced Materials* **35**, 2205927 (2023).
- <sup>18</sup>N. Sinitsyn, A. MacDonald, T. Jungwirth, V. Dugaev, and J. Sinova, "Anomalous Hall effect in a two-dimensional Dirac band: The link between the Kubo-Streda formula and the semiclassical Boltzmann equation approach," *Physical Review B* **75**, 045315 (2007).
- <sup>19</sup>B. Malaman, G. Venturini, and B. Roques, "New ternary stan- nides:  $\text{MMn}_6\text{Sn}_6$  ( $M = \text{Sc}, \text{Y}, \text{Sm}, \text{Gd}-\text{Tm}, \text{Lu}$ ) AND  $\text{ScFe}_6\text{Sn}_6$ ," *Materials research bulletin* **23**, 1629–1633 (1988).
- <sup>20</sup>S. Cheng, B. Wang, I. Lyalin, N. Bagués, A. J. Bishop, D. W. McComb, and R. K. Kawakami, "Atomic layer epitaxy of kagome magnet  $\text{Fe}_3\text{Sn}_2$  and Sn-modulated heterostructures," *APL Materials* **10**, 061112 (2022).
- <sup>21</sup>H. Rooksby and B. Lewis, "Relations between the structures of phases in the system platinum-molybdenum," *Journal of the Less Common Metals* **6**, 451–460 (1964).
- <sup>22</sup>D. Clatterbuck, R. Lange, and K. Gschneidner Jr, "Magneto-optical properties of  $\text{RMn}_6\text{Sn}_6$  ( $R = \text{Gd}, \text{Tb}, \text{Dy}, \text{Ho}, \text{Er}, \text{Tm}, \text{Lu}$ ) single crystals," *Journal of magnetism and magnetic materials* **195**, 639–645 (1999).
- <sup>23</sup>J. M. Taylor, A. Markou, E. Lesne, P. K. Sivakumar, C. Luo, F. Radu, P. Werner, C. Felser, and S. S. Parkin, "Anomalous and topological Hall effects in epitaxial thin films of the noncollinear antiferromagnet  $\text{Mn}_3\text{Sn}$ ," *Physical Review B* **101**, 094404 (2020).
- <sup>24</sup>D. Hong, N. Anand, C. Liu, H. Liu, I. Arslan, J. E. Pearson, A. Bhattacharya, and J. Jiang, "Large anomalous nernst and inverse spin-hall effects in epitaxial thin films of kagome semimetal  $\text{Mn}_3\text{Ge}$ ," *Physical Review Materials* **4**, 094201 (2020).
- <sup>25</sup>D. Khadka, T. Thapaliya, S. H. Parra, J. Wen, R. Need, J. M. Kikkawa, and S. Huang, "Anomalous Hall and Nernst effects in epitaxial films of topological kagome magnet  $\text{Fe}_3\text{Sn}_2$ ," *Physical review materials* **4**, 084203 (2020).
- <sup>26</sup>Y. Cheng, S. Yu, M. Zhu, J. Hwang, and F. Yang, "Tunable topological Hall effects in noncollinear antiferromagnet  $\text{Mn}_3\text{Sn}/\text{Pt}$  bilayers," *APL Materials* **9**, 051121 (2021).
- <sup>27</sup>K. Fujiwara, Y. Kato, H. Abe, S. Noguchi, J. Shioyai, Y. Niwa, H. Kumigashira, Y. Motome, and A. Tsukazaki, "Berry curvature contributions of kagome-lattice fragments in amorphous Fe–Sn thin films," *Nature Communications* **14**, 3399 (2023).
- <sup>28</sup>T. Thapaliya, T. Yoo, S. Hurtado Parra, N. D. Arndt, R. Need, J. M. Kikkawa, H. Kim, and S. Huang, "High-quality epitaxial thin films of topological kagome metal  $\text{CoSn}$  by magnetron sputtering," *Applied Physics Letters* **119**, 201902 (2021).
- <sup>29</sup>K. Fuchs, "The conductivity of thin metallic films according to the electron theory of metals," in *Mathematical Proceedings of the Cambridge Philosophical Society*, Vol. 34 (Cambridge University Press, 1938) pp. 100–108.
- <sup>30</sup>E. Sondheimer, "The mean free path of electrons in metals," *Advances in Physics* **1**, 1–42 (1952).
- <sup>31</sup>A. Misra, M. Hundley, D. Hristova, H. Kung, T. Mitchell, M. Nastasi, and J. Embury, "Electrical resistivity of sputtered Cu/Cr multilayered thin films," *Journal of Applied Physics* **85**, 302–309 (1999).
- <sup>32</sup>Y. Tian, L. Ye, and X. Jin, "Proper scaling of the anomalous Hall effect," *Physical review letters* **103**, 087206 (2009).